npj computational materials

www.nature.com/npjcompumats

ARTICLE OPEN

Check for updates

Effects of local compositional and structural disorder on vacancy formation in entropy-stabilized oxides from first-principles

Sieun Chae[1], Logan Williams[1], Jihang Lee[1], John T. Heron[1]✉ and Emmanouil Kioupakis[1]✉

Entropic stabilization has evolved into a strategy to create new oxide materials and realize novel functional properties engineered through the alloy composition. Achieving an atomistic understanding of these properties to enable their design, however, has been challenging due to the local compositional and structural disorder that underlies their fundamental structure-property relationships. Here, we combine high-throughput atomistic calculations and linear regression algorithms to investigate the role of local configurational and structural disorder on the thermodynamics of vacancy formation in (MgCoNiCuZn)O-based entropy-stabilized oxides (ESOs) and their influence on the electrical properties. We find that the cation-vacancy formation energies decrease with increasing local tensile strain caused by the deviation of the bond lengths in ESOs from the equilibrium bond length in the binary oxides. The oxygen-vacancy formation strongly depends on structural distortions associated with the local configuration of chemical species. Vacancies in ESOs exhibit deep thermodynamic transition levels that inhibit electrical conduction. By applying the charge-neutrality condition, we determine that the equilibrium concentrations of both oxygen and cation vacancies increase with increasing Cu mole fraction. Our results demonstrate that tuning the local chemistry and associated structural distortions by varying alloy composition acts an engineering principle that enables controlled defect formation in multi-component alloys.

npj Computational Materials (2022)8:95 ; https://doi.org/10.1038/s41524-022-00780-0

INTRODUCTION

Single-phase multicomponent metal and ceramic solid solutions have recently generated significant excitement as the large configurational entropy associated with these materials enables the stabilization of single phases of materials that are otherwise immiscible with remarkable physical properties[1–8]. Regarding ceramics, these so-called high-entropy or entropy-stabilized phases possess a large configurational entropy created through chemical disordering of one or more cation sublattices while (typically, but not necessarily[9]) the anion sublattice remains monoatomic[2]. Since their recent discovery, high-entropy oxides have demonstrated exceptional electrochemical and electronic functional properties such as a high ionic mobility[10], improved lithium storage and cyclic stability[11], efficient thermochemical water splitting at high temperature[12], magnetic exchange coupling[13], and colossal dielectric properties[14]. The proposed underlying mechanisms for these enhanced properties may involve intrinsic point defects. For example, proton[15] and Li^+ ion conduction is thought to involve vacancy-mediated diffusion[16–18], oxygen vacancies can influence light absorption and charge separation for photoelectrochemical water splitting[19], uncompensated surface spins can result from vacancies[20], and dielectric responses can be tailored through acceptor, donor, and trap states created by vacancies and defect complexes[21]. Clearly, an understanding and control of defect formation in these materials is critical for understanding their functional properties, may open doors to the discovery of, e.g., filamentary-based memristor materials[22], and shed light on diffusion-mediated processes[23,24]. Hence, the situation leads to the question: In an oxide with a large configurational entropy, how is thermodynamic defect formation influenced by the significant stereochemical disorder?

Considering an ideal chemically ordered solid, the increase in the configurational entropy is the thermodynamic driving force for the formation of point defects. In the case of multicomponent alloys with large configurational entropy, the contribution of alloy configurational entropy on the vacancy concentration remains controversial as different derivations for the equilibrium vacancy concentration are obtained using different assumptions on the variables that are conserved during vacancy formation[25,26]. A more complete description must also consider the possible variation of the formation enthalpy due to different local configurations and interactions among constituent elements, making defect formation in high-entropy materials distinct compared to low-entropy compounds[27,28].

The situation is more complicated for defects in high-entropy oxides where two distinct sublattices and charge compensation are involved. In the case of $(Mg_{0.2}Ni_{0.2}Co_{0.2}Cu_{0.2}Zn_{0.2})O$, five cations randomly populate the cation sublattice while only oxygen populates the anion sublattice. Yet, the oxygen sublattice is expected to have diverse local bond configurations since the nearest neighbors to oxygen consist of locally different combinations of the five constituent cations, while prior work has found that the oxygen sublattice experiences distortions from the ideal rocksalt structure[29,30]. Thus, point-defect formation in high-entropy oxides must consider the random local configuration in addition to the different constituent elements.

Here, we apply density functional theory calculations and statistical analysis based on linear regression to investigate point-defect formation in the entropy-stabilized oxide (ESO) $(Mg_{0.2}Ni_{0.2}Co_{0.2}Cu_{0.2}Zn_{0.2})O$, and its compositional variants, and relate it to

[1]Department of Materials Science and Engineering, University of Michigan, Ann Arbor, MI, USA. ✉email: jtheron@umich.edu; kioup@umich.edu

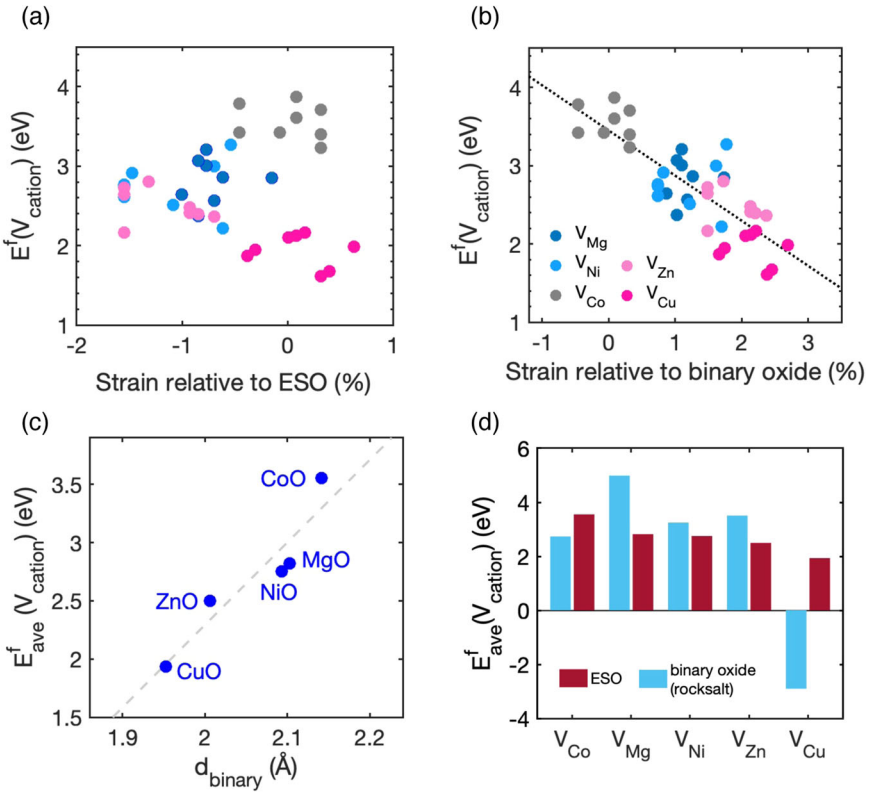

Fig. 1 Local-structure dependence of cation vacancy formation in $(Mg_{0.2}Ni_{0.2}Co_{0.2}Cu_{0.2}Zn_{0.2})O$ and comparison with binary oxides. **a**, **b** The DFT-calculated formation energies of cation vacancies in $(Mg_{0.2}Ni_{0.2}Co_{0.2}Cu_{0.2}Zn_{0.2})O$ as a function of **a** local strain relative to the average ESO bond length and **b** local strain relative to the bond length in corresponding binary oxide. The formation energies of cation vacancies decrease with increasing local strain relative to binary oxide. **c** The average formation energy of cation vacancy in ESO as a function of the average cation-oxygen bond length in corresponding binary oxides showing that the formation of cation vacancy is determined by the shift of the cation-oxygen bond distance from its equilibrium position in the binary oxides. **d** The comparison between the cation vacancy formation energy for binary oxides and the average cation vacancy formation energy for the ESO.

the local configuration and structural distortion. We also determine that charge compensation and localization in the ESO is the origin of its intrinsic electrically insulating behavior. Our results reveal the effect of stereochemical disorder, local composition fluctuations, and charge compensation on point-defect formation, which enable the engineering of the electronic and electrochemical properties of ESOs.

RESULTS

Formation energy of cation vacancies

We first calculate the formation energy of cation vacancies in their neutral charge state when no free carriers are released or consumed by holes (Methods). Here, 8 cation vacancies with different local environments are calculated for each of the 5 cation elements (thus 40 cation vacancies in total). As seen in Fig. 1a, b, we find that the formation energy of cation vacancies decreases with increasing average strain of the 6 bonds for each cation atom relative to the binary oxides (ϵ_{BO}^{rel}), but it does not correlate with the average local strain relative to the ESO (ϵ_{ESO}^{rel}) defined as:

$$\epsilon_{BO}^{rel} = \frac{1}{6}\sum_{i=1}^{6}\frac{d_{i,ESO} - d_b}{d_b} \times 100(\%), \quad (1)$$

$$\epsilon_{ESO}^{rel} = \frac{1}{6}\sum_{i=1}^{6}\frac{d_{i,ESO} - d_{ESO}}{d_{ESO}} \times 100(\%), \quad (2)$$

where $d_{i,ESO}$ is the local cation-oxygen bond length in ESO, d_b is the cation-oxygen bond length in the corresponding rocksalt binary oxide, and d_{ESO} is the average cation-oxygen bond length in the ESO. Except for Co, cation-oxygen bonds in the ESO are under tensile strain, which increases in the order of Mg, Ni, Zn, and Cu. This trend follows the average bond length of the corresponding binary oxides (Fig. 1c). We attribute the trend of decreasing cation vacancy formation energy with increasing tensile strain to the weakening of chemical bonds as the bond length increases, thus reducing the energy needed to create vacancies.

We also compared the average vacancy formation energies for each cation in the ESO to those in their binary rocksalt phases (i.e., the same crystal structure as the ESO) (Fig. 1d). We note that the Cu vacancy formation energy in CuO is negative because rocksalt CuO is thermodynamically unstable. Interestingly, the formation energies of cation vacancies in the ESO do not correlate to the values in their corresponding binary oxides. The formation energies of all cation vacancies decrease under tensile strain compared to their binary oxide phases. In a previous study, Daigle et al. evaluated the effect of chemical disorder on cation vacancy formation energy in a high-entropy diboride and related the cation vacancy concentration to the atom pair affinities and composition of cation near neighbors[31]. In our work, however, we found that both the sign as well as the magnitude of the local strain (that arises from the deviation of the metal-oxygen bond length in ESO alloys relative to the corresponding binary oxide) are decisive factors in determining the formation of cation vacancies in multicomponent crystals.

Formation energy of oxygen vacancies

Next, we calculate the formation energy of oxygen vacancies (V_O) in the neutral charge state as a function of different first-nearest-

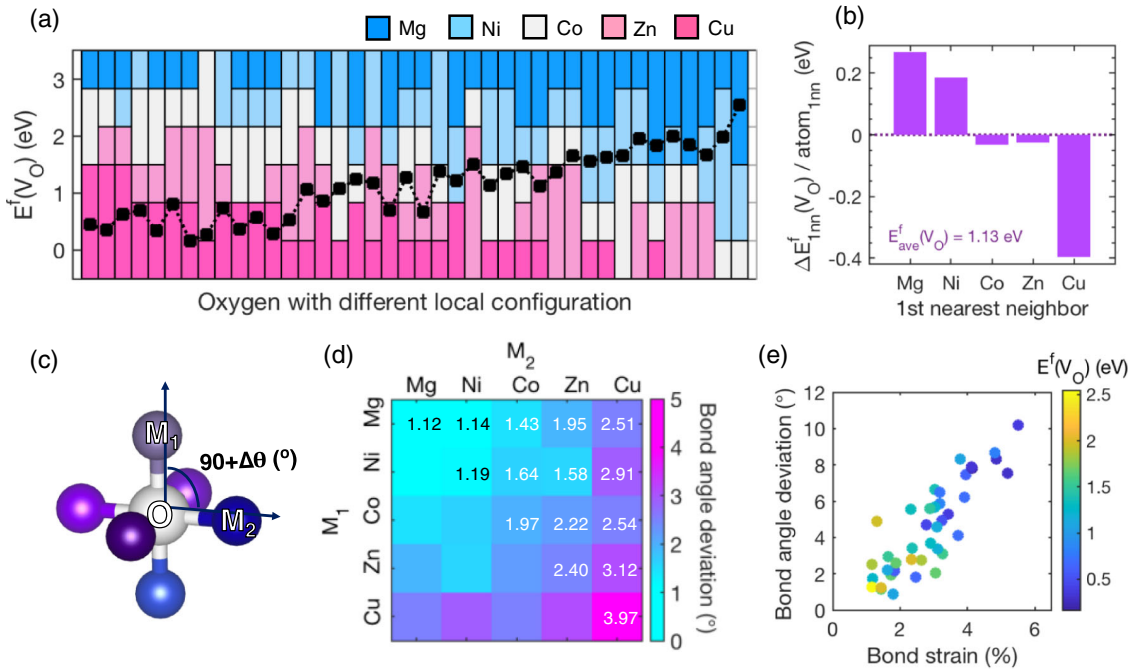

Fig. 2 Dependence of the oxygen-vacancy formation energy on the local configuration and structural distortion in ($Mg_{0.2}Ni_{0.2}Co_{0.2}Cu_{0.2}Zn_{0.2}$)O. a DFT-calculated formation energy of oxygen vacancy (V_O) as a function of first-nearest-neighbor (1NN) shell composition. Each column represents a different oxygen atom in the cell and the cation combination for each 1NN shell is illustrated by the colored bars in the background. The data is ordered along the horizontal axis according to E^f from our linear regression analysis. **b** The contribution of each 1NN cation to the oxygen vacancy formation, obtained by fitting the DFT-calculated V_O formation energies to the number of each 1NN cation with the linear-regression scheme. The formation energy of V_O strongly depends on the local atomic configuration: it increases with an increasing number of Mg and Ni 1NN cations, and it decreases with more Cu 1NN cations. **c** Schematic of the octahedral arrangement of O in ESO, where the six 1NN cation sites are determined by the combination of the five cation species. Different combinations of cations lead to different local bond-angle deviations, $\Delta\theta$ (°) **d** The values of the average M_1-O-M_2 bond-angle deviation from 90°, where M_1 and M_2 indicate metal cations in the ESO. Cu (Mg) contributes the most (least) to the distortion of bond angle. **e** The formation energy of V_O as a function of average bond-angle deviation and average bond strain. The local structural distortion, determined by local bond strain and bond-angle deviation, decreases the formation energy of V_O's and increases their formation probability.

neighbor (1NN) shell compositions (Fig. 2a). Due to the finite supercell size, 40 different combinations of the 210 possible combinations of the 1NN shell are calculated. V_O formation energies range from 0.17 eV to 2.54 eV and strongly dependent on the local configuration. To evaluate the contribution of each 1NN cation to the formation of the V_O, the calculated formation energies ($E^f_{DFT}(V_O)$) are fitted using linear regressions over the five input variables (N_{Ni}, N_{Mg}, N_{Co}, N_{Zn}, N_{Cu}) that describe the number of atoms of each cation species surrounding the oxygen site:

$$E^f_{LR}(V_O) = E^f_{ave} + \Delta E^f_{1NN,Ni}\cdot N_{Ni} + \Delta E^f_{1NN,Mg}\cdot N_{Mg} + \Delta E^f_{1NN,Co}\cdot N_{Co} + \Delta E^f_{1NN,Zn}\cdot N_{Zn} + \Delta E^f_{1NN,Cu}\cdot N_{Cu}, \quad (3)$$

where $E^f_{LR}(V_O)$ denotes the site-dependent formation energy of the ESO that depends on the local cation composition (not a linearly averaged formation energy for the entire system), E^f_{ave} the intercept term underlying the average V_O formation energy in the ESO, and ΔE^f_{1NN} the model parameter value assigned to each variable. The correlation between $E^f_{DFT}(V_O)$ and $E^f_{LR}(V_O)$ is shown in Supplementary Fig. 1a. The correlation is determined by the root-mean-square error (RMSE) between $E^f_{DFT}(V_O)$ and $E^f_{LR}(V_O)$, which is computed to be 0.235 eV. ΔE^f_{1NN} for each cation is plotted in Fig. 2b. We find positive ΔE^f_{1NN} values for Mg and Ni, and a large negative value for Cu, implying that oxygen vacancies are more (less) likely to form in a Cu- (Mg- or Ni-) rich local environment. We obtain negative ΔE^f_{1NN} values for Zn and Co, however, the values are relatively small. Using our linear regression model, the distribution of $E^f(V_O)$ is obtained for all 210 possible combinations of 1NN shells (Supplementary Fig. 1b), which shows a large variation of the $E^f(V_O)$ (from –0.8 eV to 2.4 eV) resulting from local configurational disorder.

The contribution of a 1NN cation to the V_O formation energy correlates with the local lattice distortion, which is characterized by the local bond-angle deviation from 90° (the ideal bond angle for the rocksalt structure) and bond strain. Figure 2d illustrates the average cation-oxygen-cation bond angle deviation for the various combinations of cations calculated from the relaxed DFT structure of ($Mg_{0.2}Ni_{0.2}Co_{0.2}Cu_{0.2}Zn_{0.2}$)O. The local bond angle distorts the most for Cu, followed by Zn, Co, Ni, and Mg 1NN cations, in decreasing order, where the maximum average bond-angle deviation is observed for the Cu-O-Cu bond (3.97 °) and the minimum is for Mg-O-Mg (1.12 °). Figure 2e plots $E^f(V_O)$ against the average bond-angle deviation and the average bond strain of the six bonds in an octahedron, revealing the correlation between local lattice distortion and $E^f(V_O)$. $E^f(V_O)$ is linearly fitted with the average bond-angle deviation and the average bond strain, separately, in Supplementary Fig. 1c, d. The correlation defined by the root mean square error between $E^f(V_O)$ and the average bond angle deviation/strain is computed to be 0.4567 eV/0.4092 eV, which corresponds to a relative error of 19%. Our results therefore demonstrate that the formation energy of oxygen vacancies is related both to the local bond-angle deviation and to the local strain, which stem from the strain of the cation-oxygen bonds in chemically disordered ESOs relative to the binaries.

Thermodynamic transition levels of vacancies

We further investigate the electronic properties of vacancies in equimolar $Mg_{0.2}Ni_{0.2}Co_{0.2}Cu_{0.2}Zn_{0.2}O$. Among various structural configurations, we chose oxygen and cation vacancies with the lowest formation energies and calculate their stable charge states.

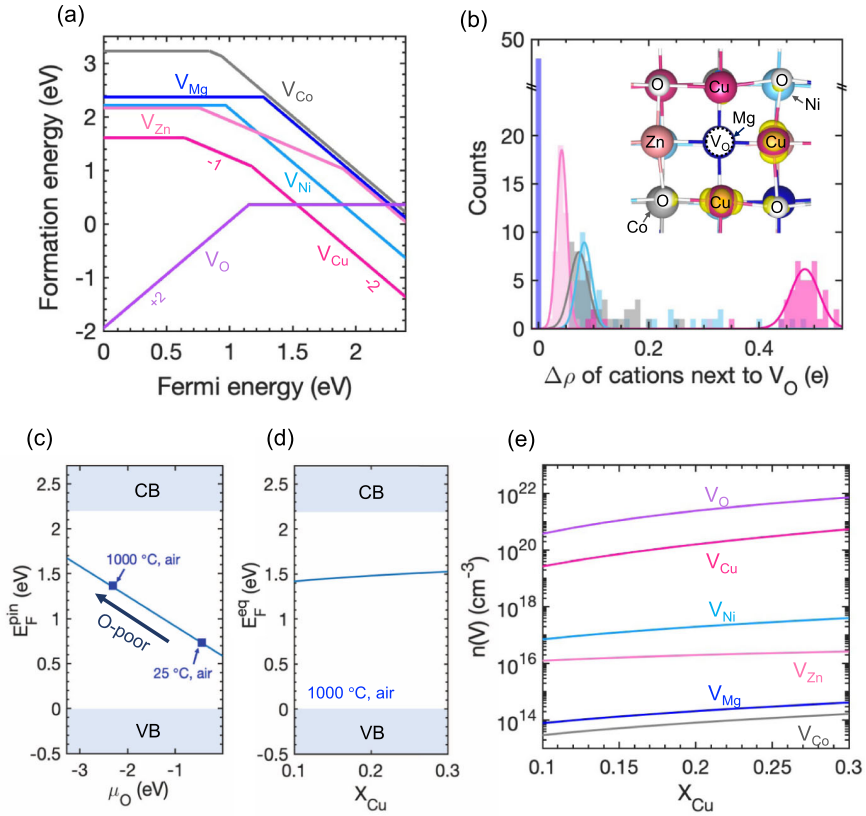

Fig. 3 Charge compensation and localization from point defects in $(Mg_{0.2}Ni_{0.2}Co_{0.2}Cu_{0.2}Zn_{0.2})O$. a Formation energy of oxygen and cation vacancies as a function of Fermi level assuming bulk growth conditions (1000 °C, air). An oxygen vacancy is a deep donor while cation vacancies are deep acceptors. **b** The histogram and fits of the change in Bader charge of 1NN cations before and after the formation of an oxygen vacancy. The inset illustrates the local atomic structure of the entropy-stabilized oxide with the lowest-formation-energy oxygen vacancy and the isosurface of the band-decomposed charge density at the conduction band minimum (CBM). The value of the isosurface is chosen to be 50% of the charge density. The charge distribution of excess electrons from an oxygen vacancy (yellow) is localized on the nearest Cu atoms. **c** Calculated Fermi-level pinning energy as a function of oxygen chemical potential. The characteristic oxygen chemical potential and Fermi level pinning energy under bulk (1000 °C, air) synthesis conditions as well as standard ambient temperature and pressure (25 °C, air) are specified. Under typical growth conditions, the Fermi energy is pinned at a deep energy level within the band gap, in agreement with the observation of the electrically insulating state of $(Mg_{0.2}Ni_{0.2}Co_{0.2}Cu_{0.2}Zn_{0.2})O$. **d** Calculated equilibrium Fermi energy level as a function of Cu mole fraction. The mole fraction for the non-variable cations equally composes the remaining mole fraction. Increasing Cu composition leads to increased charged oxygen vacancy formation, which enhances the equilibrium Fermi level toward CBM. **e** Calculated equilibrium vacancy concentration of oxygen and cations as a function of Cu mole fraction. By utilizing the local configuration effect on oxygen vacancy formation energy and the subsequent cation vacancy formation for charge neutrality, the vacancy density of ESO can be tuned by cation mole fraction.

Figure 3a shows the formation energy (E^f) of vacancies in the ESO in their dominant charge states as a function of the Fermi energy (E_F) level at the characteristic growth condition for bulk synthesis (1000 °C in air)[2]. We find that V_O is a deep donor defect with the +2/0 thermodynamic transition level at $E_F = 1.239$ eV below the CBM. V_{Cu}, V_{Zn}, and V_{Co} are stable in the 0, −1, or −2 charge states while V_{Mg} and V_{Ni} are only stable in the 0 or −2 charge states, depending on the Fermi level. All cation vacancies are deep acceptors with acceptor ionization energies spanning from 0.658 eV (for V_{Cu}) to 1.271 eV (for V_{Mg}).

We also investigate the charge distribution of electrons bound to oxygen vacancies in the neutral charge state. The inset of Fig. 3b illustrates the band-decomposed charge density for electrons bound to the oxygen vacancy with the lowest formation energy. The electrons localize around the 1NN Cu atoms. In order to extend our analysis to all oxygen vacancies in our supercell, we calculated the change of the Bader charges of the 1NN cations before and after the formation of V_O (Fig. 3b)[32–35]. We find that the electron density around the neighboring Cu changes the most, by 0.47 e on average, while the electron density around Mg remains relatively unchanged (0.00037 e on average), and the charge states of Zn, Co, and Ni change by 0.04 e, 0.07 e, 0.09 e on average, respectively. Since the Cu 3d orbitals contribute the most (91%) to the conduction band minimum (CBM) wave function of the ESO, we anticipate that the conduction mechanism of the ESO to be dominated by variable-range electron hopping between localized Cu states.

Equilibrium Fermi level and vacancy concentration

The equilibrium Fermi level is determined by the interplay of extra electrons released by positively charged V_O and consumed by negatively charged cation vacancies. We identify the Fermi level pinning position (E_F^{pin}) to be the crossing point between V_O^{2+} and V_{Cu}^{2-} in the E^f vs E_F diagram, which are the two dominant vacancies in the ESO. Since the concentration of vacancies at different charge states is affected by the synthesis conditions, with E_F^{pin} changing accordingly, we calculate E_F^{pin} according to the oxygen chemical potential (μ_O) and plot it in Fig. 3c. We also specify the μ_O at the conditions for typical bulk ESO synthesis (1000 °C in air) and standard temperature and pressure. Reducing μ_O (oxygen-poor conditions) lowers the formation energy of V_O^{2+}

and increases E_F^{pin} while the opposite is found for increasing values of μ_O. However, we determine E_F^{pin} is a deep level within the band gap for the μ_O values under typical synthesis conditions, indicating that $(Mg_{0.2}Ni_{0.2}Co_{0.2}Cu_{0.2}Zn_{0.2})O$ is intrinsically electrically insulating.

We then calculate the equilibrium oxygen and cation vacancy concentration as a function of cation composition, particularly the Cu composition. As the formation energy of a cation vacancy is cation-type specific and does not show strong correlation with local configuration, we select the lowest vacancy formation energy for each cation species to calculate the equilibrium cation-vacancy concentrations. We assumed element-specific vacancy types and negligible contribution from mixing entropy[26], and calculated each cation vacancy concentration using the Maxwell-Boltzmann equation:

$$n(V_{cation}) = N_{cation} \cdot P \cdot \exp\left(-\frac{E^f(V_{cation})}{k_B T}\right), \quad (4)$$

where P is the chemically weighted site density by treating each cation vacancy as a separate species.

On the other hand, we applied our linear regression model ($E^f_{LR}(V_O)$) to model $E^f(V_O{}^0)$ as well as $E^f(V_O{}^{2+})$. As our calculations show that the charge transition level (E_t) of V_O varies relatively little (<0.2 eV) depending on the local configuration, we assume the charge-transition level of V_O is the same for all O sites and modeled $E^f(V_O{}^{2+})$ according to:

$$E^f\left(V_O^{2+}\right) = E^f_{LR}(V_O) + 2(E_F - E_t), \quad (5)$$

By assuming configurational homogeneity without local ordering (as previously demonstrated in ref. [29]) and considering all possible local configurations, the equilibrium oxygen vacancy concentration in both the neutral and the +2 charge state in compositionally varied ESOs (e.g., $Mg_{0.25(1-x)}Co_{0.25(1-x)}Ni_{0.25(1-x)}Cu_xZn_{0.25(1-x)}O$) is calculated using:

$$n(V_O) = \sum_i N_O \cdot P_i \cdot \exp\left(-\frac{E^f_{LR,i}(V_O)}{k_B T}\right), \quad (6)$$

where N_O is the number of oxygen sites, P_i is the probability of the i^{th} 1NN configuration (see Methods), $E^f_{LR,i}(V_O)$ is the calculated oxygen vacancy formation energy for the i^{th} 1NN configuration, k_B is the Boltzmann constant, and T is the synthesis temperature. Vacancies with 1NN configurations that result in a negative formation energy (e.g., 93% of the vacancy configurations with more than four 1NN Cu) are assumed to form spontaneously. Then, the charge-neutrality condition is applied to calculate the equilibrium Fermi energy (E_F^{eq}), and the equilibrium vacancy concentrations of oxygen and cations are calculated as a function of Cu mole fraction, x_{Cu}. Figure 3d plots E_F^{eq} a function of x_{Cu} and Fig. 3e plots the equilibrium vacancy concentrations of oxygen and cations a function of x_{Cu}, while the mole fraction of the other cations is $0.25(1–x_{Cu})$, for T = 1000 °C. The V_O concentration increases significantly as the Cu mole fraction increases. Also, though the increased V_{Cu} with increasing x_{Cu} introduces more holes, E_F^{eq} increases toward the CBM as the larger number of electrons are introduced from oxygen vacancies with increasing x_{Cu}. This result shows that increasing the Cu mole fraction increases both the O vacancy and the Cu vacancy concentrations at an approximately constant ratio, independent of alloy composition, due to the charge compensation between these two dominant vacancy species.

DISSCUSSION

Among the wide-ranging applications, ESOs have been particularly studied as energy-storage materials owing to the high capacity retention and Li-extraction ability of the compound[11,36,37]. According to the proposed mechanism, Li^+ insertion/extraction occurs via the conduction path which involves oxygen vacancies[10], and Li^+/Li conversion occurs inside the compound via the redox reaction with some of the cations in ESOs (e.g., Co^{2+}, Cu^{2+})[11]. A defect-rich structure allows the formation of Li_2O nuclei while keeping the structure of the host matrix intact throughout cycling, which ensures the reversibility of the reaction[11]. Defects can also facilitate Li superionic conduction, which allows high discharge capacity. The proposed mechanism indicates that selecting/tuning the composition to design ESO with abundant oxygen vacancies and redox-active species by, e.g., increasing the Cu composition, is an effective strategy to improve the electrochemical performance of ESOs[38].

In addition, cation-valence engineering by tuning the concentration of oxygen vacancies can affect the functional properties of ESOs. Particularly, variations to the Co charge state directly influence the magnetic transitions of ESOs as Co^{2+} (d^7) is a magnetic cation whereas Co^{3+} (d^6) is magnetically inert[39]. Kotsonis et al.[40] observed an increase in Co^{3+} by reducing the film-growth temperature, which leads to magnetic dilution of the system. According to our analysis, the observed charge-state change of Co is expected to be associated with reduced oxygen vacancy concentration at lower growth temperatures.

To conclude, we investigated the thermodynamic and electronic properties of cation and oxygen vacancies in entropy-stabilized oxides. We uncovered design rules for controlled vacancy formation by tuning the cation composition. We found that the local compositional variations in ESOs give rise to structural distortions and strain, arising from the deviation of the cation-oxygen bond lengths relative to the binaries, play a decisive role in the formation of both cation and oxygen vacancies. Based on a linear-regression analysis of the first-principles results, we developed a model to predict the oxygen vacancy density as a function of cation composition. Our results provide useful guidance to identify thermodynamically preferred defect sites and engineer the vacancy formation in multi-component alloys.

METHOD

Density functional theory calculation

We performed first-principles calculations based on density functional theory using the projector augmented wave (PAW) method and generalized gradient approximation (GGA) functionals as implemented in the Vienna Ab initio Simulation Package (VASP)[41–43]. The PAW pseudopotentials including the Mg $3s^2$, Co $3d^74s^2$, Ni $3d^84s^2$, Cu $3d^{10}4s^1$, Zn $3d^{10}4s^2$ and O $2s^22p^4$ electrons as the valence state were employed, and the plane-wave cut-off energy was set to 400 eV. To better predict the localized characteristics of the d-electron shell, on-site Coulomb interaction corrections were applied for the transition metal atoms using the DFT + Hubbard U formalism[44]. In this approach, the Hubbard U parameter is chosen from the Automatic-Flow (AFLOW) standard for high-throughput construction of materials science and electronic structure database[45], which is 5, 5.1, 4.0, and 7.5 eV for Co, Ni, Cu, and Zn, respectively. All structures are relaxed using a conjugate-gradient algorithm. The maximal force criterion of 0.01 eV/Å was used for the ionic relaxation and a maximal energy criterion of 10^{-8} eV was used for the electronic self-consistent loop.

We modeled the $(Mg_{0.2}Co_{0.2}Ni_{0.2}Cu_{0.2}Zn_{0.2})O$ entropy-stabilized oxide and its compositional variants using 80-atom supercells and Γ-centered $2 \times 2 \times 2$ Brillouin-zone sampling grids. The alloy randomness is modeled using Special Quasi-random Structures (SQS)[46], generated with the Alloy Theoretic Automated Toolkit[47] to match the pair correlation functions of the random solid solution up to a radius of 6 Å. As the magnetic structure of the rocksalt (MgCoNiCuZn)O is antiferromagnetic in its ground state, we also considered the arrangement of atomic spins where (111) planes contain magnetic moments alternatively parallel and antiparallel with the spin direction along [211][13,48,49]. Each cation is equally populated in the two magnetic sites: $(Mg_{0.2}Co^{\uparrow}_{0.1}Co^{\downarrow}_{0.1}Ni^{\uparrow}_{0.1}Ni^{\downarrow}_{0.1}Cu^{\uparrow}_{0.1}Cu^{\downarrow}_{0.1}Zn_{0.2})O$. The lattice constant is determined from the energy minimum. The band gap is corrected using a linear correction scheme we designed that is based on

the scissor-shift method; the valence-band maximum (VBM) and the conduction-band minimum (CBM) for the constituent binary oxides (rocksalt structure for MgO, CoO, NiO, and ZnO, and tenorite structure for CuO) are calculated using the GGA + U and the HSE06[50] functionals, and the average energy difference between the VBM (or CBM) states calculated with GGA + U and with HSE06 is used to correct the VBM (or CBM) energy of the ESO (Supplementary Fig. 2). Although we expect that the presence of alloy disorder can lead to band bowing and the reduction in the band gap compared to our linear correction scheme, our results on $Mg_{0.5}Zn_{0.5}O$ alloy shows that our method gives an error bar for the VBM and CBM corrections by less than 0.1 eV. Since both cation and oxygen vacancies in ESOs are predicted to be deep defects with ionization energies higher than 0.65 eV, we expect that the bowing of the band edges by an amount on the order of a few 100 meV does not affect their predicted deep nature. We also construct 64-atom supercells for rocksalt MgO, CoO, NiO, ZnO, and CuO to calculate the formation energy of cation vacancies in binary oxides. The metastable rocksalt structure CuO was calculated by relaxing the unit-cell volume and ionic positions while maintaining the symmetry.

The formation energy of a point defect D in charge state q is defined by[51]

$$E^f(D^q) = E_{\mathrm{tot}}(D^q) - E_{\mathrm{tot}}(\mathrm{bulk}) - \sum n_i(E_i + \mu_i) + \mathrm{q}(E_F + E_v) + E_{\mathrm{corr}}(D^q), \tag{7}$$

where $E_{\mathrm{tot}}(D^q)$ is the total energy of a supercell with a point defect, $E_{\mathrm{tot}}(\mathrm{bulk})$ is the total energy of a reference supercell without a point defect, n_i is the number of defect atoms added to or removed from the supercell, E_i is the energy per atom in its elemental phase, μ_i is the chemical potential, E_F is the Fermi level, E_v is the valence-band maximum, and $E_{\mathrm{corr}}(D^q)$ is the correction energy arising from defect-defect interaction due to the finite supercell size, which is calculated with the SXDFECTA-LIGN[52] code. For the correction energy, we set the static dielectric constant of the ESO to $\varepsilon_0 = 17.99$, which was determined by density functional perturbation theory[53].

The chemical potential of the defect species depends on the growth temperature and pressure. We choose typical bulk synthesis conditions of ESO ($T = 1000$ °C in air) and calculate the oxygen chemical potential, $\mu_O = -2.306$ eV, using the following equation:

$$\mu(P,T) = k_B T \ln(nV_Q) = k_B T \ln\left(\frac{P}{RT}V_Q\right) \tag{8}$$

where k_B is the Boltzmann constant, n is the density of O_2, V_Q is the quantum volume of O_2, and R is the ideal gas constant. The chemical potentials for the cation species are also limited by the formation of secondary phases such as MgO, Co_3O_4, NiO, ZnO, and Cu_2O. The derivation and actual values for the chemical potentials are described in Supplementary Tables 1 and 2.

Probability of the local configuration

There are 210 combinations that the five distinct cations can occupy the 6 nearest neighbor sites of oxygen. The probability of the local configuration is determined by:

$$P = \frac{6!}{n_{Ni}! \cdot n_{Mg}! \cdot n_{Co}! \cdot n_{Zn}! \cdot n_{Cu}!} x_{Ni}^{n_{Ni}} \cdot x_{Mg}^{n_{Mg}} \cdot x_{Co}^{n_{Co}} \cdot x_{Zn}^{n_{Zn}} \cdot x_{Cu}^{n_{Cu}} \tag{9}$$

where n_{Ni}, n_{Mg}, n_{Co}, n_{Zn}, and n_{Cu} are the number of atoms of the Ni, Mg, Co, Zn, and Cu cation constituents in the nearest neighbor sites to the oxygen atom, and x_{Ni}, x_{Mg}, x_{Co}, x_{Zn}, and x_{Cu} are the Ni, Mg, Co, Zn, and Cu mole fractions in the ESO, respectively.

DATA AVAILABILITY

The data that support the findings of this study are available from the corresponding authors upon reasonable request.

Received: 4 November 2021; Accepted: 4 April 2022;
Published online: 29 April 2022

REFERENCES

1. Miracle, D. B. & Senkov, O. N. A critical review of high entropy alloys and related concepts. *Acta Mater.* **122**, 448–511 (2017).
2. Rost, C. M. et al. Entropy-stabilized oxides. *Nat. Commun.* **6**, 8485 (2015).
3. Sarkar, A. et al. High-entropy oxides: fundamental aspects and electrochemical properties. *Adv. Mater.* **31**, 1806236 (2019).
4. Sarker, P. et al. High-entropy high-hardness metal carbides discovered by entropy descriptors. *Nat. Commun.* **9**, 4980 (2018).
5. Gild, J. et al. High-entropy metal diborides: a new class of high-entropy materials and a new type of ultrahigh temperature ceramics. *Sci. Rep.* **6**, 2–11 (2016).
6. Oses, C., Toher, C. & Curtarolo, S. High-entropy ceramics. *Nat. Rev. Mater.* **5**, 295–309 (2020).
7. Meisenheimer, P. B. & Heron, J. T. Oxides and the high entropy regime: a new mix for engineering physical properties. *MRS Adv.* **5**, 3419–3436 (2020).
8. Musicó, B. L. et al. The emergent field of high entropy oxides: design, prospects, challenges, and opportunities for tailoring material properties. *APL Mater.* **8**, 040912 (2020).
9. Deng, Z. et al. Semiconducting high-entropy chalcogenide alloys with ambi-ionic entropy stabilization and ambipolar doping. *Chem. Mater.* **32**, 6070–6077 (2020).
10. Bérardan, D., Franger, S., Meena, A. K. & Dragoe, N. Room temperature lithium superionic conductivity in high entropy oxides. *J. Mater. Chem. A* **4**, 9536–9541 (2016).
11. Sarkar, A. et al. High entropy oxides for reversible energy storage. *Nat. Commun.* **9**, 3400 (2018).
12. Zhai, S. et al. The use of poly-cation oxides to lower the temperature of two-step thermochemical water splitting. *Energy Environ. Sci.* **11**, 2172–2178 (2018).
13. Meisenheimer, P. B., Kratofil, T. J. & Heron, J. T. Giant enhancement of exchange coupling in entropy-stabilized oxide heterostructures. *Sci. Rep.* **7**, 3–8 (2017).
14. Bérardan, D., Franger, S., Dragoe, D., Meena, A. K. & Dragoe, N. Colossal dielectric constant in high entropy oxides. *Phys. Status Solidi Rapid Res. Lett.* **10**, 328–333 (2016).
15. Rowberg, A. J. E., Weston, L. & Van De Walle, C. G. Optimizing proton conductivity in zirconates through defect engineering. *ACS Appl. Energy Mater.* **2**, 2611–2619 (2019).
16. Hoang, K. Defect physics, delithiation mechanism, and electronic and ionic conduction in layered lithium manganese oxide cathode materials. *Phys. Rev. Appl.* **3**, 024013 (2015).
17. Lu, Z. et al. Defect chemistry and lithium transport in Li3OCl anti-perovskite superionic conductors. *Phys. Chem. Chem. Phys.* **17**, 32547–32555 (2015).
18. He, X., Zhu, Y. & Mo, Y. Origin of fast ion diffusion in super-ionic conductors. *Nat. Commun.* **8**, 15893 (2017).
19. Kim, M. et al. Oxygen-vacancy-introduced BaSnO3−δ photoanodes with tunable band structures for efficient solar-driven water splitting. *Adv. Mater.* **31**, 1903316 (2019).
20. Berkowitz, A. E. & Takano, K. Exchange anisotropy—a review. *J. Magn. Magn. Mater.* **200**, 552–570 (1999).
21. Saremi, S. et al. Enhanced electrical resistivity and properties via ion bombardment of ferroelectric thin films. *Adv. Mater.* **28**, 10750–10756 (2016).
22. Lee, J. & Lu, W. D. On-demand reconfiguration of nanomaterials: when electronics meets ionics. *Adv. Mater.* **30**, 1702770 (2018).
23. Grzesik, Z. et al. Defect structure and transport properties in (Co,Cu,Mg,Ni,Zn)O high entropy oxide. *J. Eur. Ceram. Soc.* **39**, 4292–4298 (2019).
24. Osenciat, N. et al. Charge compensation mechanisms in Li-substituted high-entropy oxides and influence on Li superionic conductivity. *J. Am. Ceram. Soc.* **102**, 6156–6162 (2019).
25. Ruban, A. V. Thermal vacancies in random alloys in the single-site mean-field approximation. *Phys. Rev. B* **93**, 134115 (2016).
26. Morgan, D. & Zhang, Y. Comment on 'Thermal vacancies in random alloys in the single-site mean-field approximation'. *Phys. Rev. B* **101**, 136101 (2020).
27. Li, C. et al. First principle study of magnetism and vacancy energetics in a near equimolar NiFeMnCr high entropy alloy. *J. Appl. Phys.* **125**, 155103 (2019).
28. Piochaud, J. B. et al. First-principles study of point defects in an fcc Fe-10Ni-20Cr model alloy. *Phys. Rev. B Condens. Matter Mater. Phys.* **89**, 024101 (2014).
29. Rost, C. M., Rak, Z., Brenner, D. W. & Maria, J. P. Local structure of the MgxNixCoxCuxZnxO(x=0.2) entropy-stabilized oxide: An EXAFS study. *J. Am. Ceram. Soc.* **100**, 2732–2738 (2017).
30. Anand, G., Wynn, A. P., Handley, C. M. & Freeman, C. L. Phase stability and distortion in high-entropy oxides. *Acta Mater.* **146**, 119–125 (2018).
31. Daigle, S. E. & Brenner, D. W. Statistical approach to obtaining vacancy formation energies in high-entropy crystals from first principles calculations: Application to a high-entropy diboride. *Phys. Rev. Mater.* **4**, 123602 (2020).
32. Henkelman, G., Arnaldsson, A. & Jónsson, H. A fast and robust algorithm for Bader decomposition of charge density. *Comput. Mater. Sci.* **36**, 354–360 (2006).
33. Sanville, E., Kenny, S. D., Smith, R. & Henkelman, G. Improved grid-based algorithm for bader charge allocation. *J. Comput. Chem.* **28**, 899–908 (2007).
34. Tang, W., Sanville, E. & Henkelman, G. A grid-based Bader analysis algorithm without lattice bias. *J. Phys. Condens. Matter* **21**, 084204 (2009).
35. Yu, M. & Trinkle, D. R. Accurate and efficient algorithm for Bader charge integration. *J. Chem. Phys.* **134**, 064111 (2011).

36. Wang, Q. et al. Multi-anionic and -cationic compounds: new high entropy materials for advanced Li-ion batteries. *Energy Environ. Sci.* **12**, 2433–2442 (2019).
37. Zhao, C., Ding, F., Lu, Y., Chen, L. & Hu, Y. S. High-entropy layered oxide cathodes for sodium-ion batteries. *Angew. Chem. Int. Ed.* **59**, 264–269 (2020).
38. Lökçü, E., Toparli, Ç. & Anik, M. Electrochemical performance of (MgCoNiZn)1-xLixO high-entropy oxides in lithium-ion batteries. *ACS Appl. Mater. Interfaces* **12**, 23860–23866 (2020).
39. Meisenheimer, P. B. et al. Magnetic frustration control through tunable stereochemically driven disorder in entropy-stabilized oxides. *Phys. Rev. Mater.* **3**, 104420 (2019).
40. Kotsonis, G. N. et al. Property and cation valence engineering in entropy-stabilized oxide thin films. *Phys. Rev. Mater.* **4**, 100401 (2020).
41. Kresse, G. & Hafner, J. Ab initio molecular dynamics for liquid metals. *Phys. Rev. B* **47**, 558–561 (1993).
42. Kresse, G. & Furthmüller, J. Efficient iterative schemes for ab initio total-energy calculations using a plane-wave basis set. *Phys. Rev. B Condens. Matter Mater. Phys.* **54**, 11169–11186 (1996).
43. Kresse, G. & Furthmüller, J. Efficiency of ab-initio total energy calculations for metals and semiconductors using a plane-wave basis set. *Comput. Mater. Sci.* **6**, 15–50 (1996).
44. Anisimov, V. I., Zaanen, J. & Andersen, O. K. Band theory and Mott insulators: hubbard U instead of stoner I. *Phys. Rev. B* **44**, 943–954 (1991).
45. Calderon, C. E. et al. The AFLOW standard for high-throughput materials science calculations. *Comput. Mater. Sci.* **108**, 233–238 (2015).
46. Zunger, A., Wei, S.-H., Ferreira, L. G. & Bernard, J. E. Special quasirandom structures. *Phys. Rev. Lett.* **65**, 353–356 (1990).
47. Van De Walle, A. et al. Efficient stochastic generation of special quasirandom structures. *Calphad* **42**, 13–18 (2013).
48. Jimenez-Segura, M. P. et al. Long-range magnetic ordering in rocksalt-type high-entropy oxides. *Appl. Phys. Lett.* **114**, 122401 (2019).
49. Zhang, J. et al. Long-range antiferromagnetic order in a rocksalt high entropy oxide. *Chem. Mater.* **31**, 3705–3711 (2019).
50. Heyd, J., Scuseria, G. E. & Ernzerhof, M. Hybrid functionals based on a screened Coulomb potential. *J. Chem. Phys.* **118**, 8207–8215 (2003).
51. Freysoldt, C. et al. First-principles calculations for point defects in solids. *Rev. Mod. Phys.* **86**, 253–305 (2014).
52. Freysoldt, C., Neugebauer, J. & Van De Walle, C. G. Fully Ab initio finite-size corrections for charged-defect supercell calculations. *Phys. Rev. Lett.* **102**, 016402 (2009).
53. Baroni, S. et al. Perturbation theory. *Rev. Mod. Phys.* **73**, 515–562 (2001).

ACKNOWLEDGEMENTS

The oxygen vacancy work was supported by NSF grant DMR-1810119. The cation vacancy work was supported by NSF CAREER grant DMR-1847847. J.T.H. acknowledges support from NSF MRSEC DMR-2011839. Computational resources were provided by the DOE NERSC facility (DE-AC02-05CH11231).

AUTHOR CONTRIBUTIONS

S.C. performed first principles calculations, analyzed data, and wrote the paper under the supervision of J.T.H. and E.K. L.W. and J.L. assisted analyzing the data. E.K. and J.T.H. supervised the calculation, analysis, and manuscript preparation. All contributors proofread the manuscript.

COMPETING INTERESTS

The authors declare no competing interests.

ADDITIONAL INFORMATION

Supplementary information The online version contains supplementary material available at https://doi.org/10.1038/s41524-022-00780-0.

Correspondence and requests for materials should be addressed to John T. Heron or Emmanouil Kioupakis.

Reprints and permission information is available at http://www.nature.com/reprints

Publisher's note Springer Nature remains neutral with regard to jurisdictional claims in published maps and institutional affiliations.